JGR Solid Earth

RESEARCH ARTICLE
10.1029/2023JB027348

Adjoint-State Teleseismic Traveltime Tomography: Method and Application to Thailand in Indochina Peninsula

Jing Chen[1], Shucheng Wu[1,2], Mijian Xu[1], Masaru Nagaso[1], Jiayuan Yao[3], Kai Wang[4], Tianjue Li[1], Yiming Bai[1], and Ping Tong[1,2,5]

[1]Division of Mathematical Sciences, School of Physical and Mathematical Sciences, Nanyang Technological University, Singapore, Singapore, [2]Earth Observatory of Singapore, Nanyang Technological University, Singapore, Singapore, [3]State Key Laboratory of Geological Processes and Mineral Resources, School of Geophysics and Geomatics, China University of Geosciences, Wuhan, China, [4]School of Earth and Space Sciences, University of Science and Technology of China, Hefei, China, [5]Asian School of the Environment, Nanyang Technological University, Singapore, Singapore

Key Points:

- A novel framework based on the adjoint-state method is developed for teleseismic traveltime tomography
- The low-velocity anomalies beneath the southern and western margins of Khorat Plateau suggest mantle upwelling due to mantle convection
- The existence of mantle upwelling indicates lithospheric modification beneath the Khorat Plateau

Supporting Information:

Supporting Information may be found in the online version of this article.

Correspondence to:

P. Tong,
tongping@ntu.edu.sg

Citation:

Chen, J., Wu, S., Xu, M., Nagaso, M., Yao, J., Wang, K., et al. (2023). Adjoint-state teleseismic traveltime tomography: Method and application to Thailand in Indochina Peninsula. *Journal of Geophysical Research: Solid Earth*, *128*, e2023JB027348. https://doi.org/10.1029/2023JB027348

Received 26 JUN 2023
Accepted 6 DEC 2023

Author Contributions:

Data curation: Jiayuan Yao
Formal analysis: Jing Chen, Shucheng Wu, Mijian Xu
Funding acquisition: Ping Tong
Methodology: Jing Chen, Tianjue Li, Ping Tong
Project Administration: Ping Tong
Resources: Jiayuan Yao
Software: Jing Chen, Masaru Nagaso, Ping Tong
Supervision: Ping Tong
Validation: Jing Chen, Masaru Nagaso
Visualization: Jing Chen
Writing – original draft: Jing Chen, Shucheng Wu, Mijian Xu
Writing – review & editing: Shucheng Wu, Mijian Xu, Jiayuan Yao, Kai Wang, Tianjue Li, Yiming Bai, Ping Tong

Abstract We propose a novel framework for teleseismic traveltime tomography that requires no ray tracing. The tomographic inverse problem is formulated as an Eikonal equation-constrained optimization problem, aiming at the determination of a slowness model that minimizes the difference between observational and predicted differential traveltimes. Two improvements have been made over previous ray-based methods. First, the traveltimes from the source outside the study region to any positions within the study region are computed using a hybrid approach. This involves solving a 2D Eikonal equation to obtain the traveltimes from the source to the boundary of the study region and solving a 3D Eikonal equation to compute the traveltimes from the boundary to any positions within the study region. Second, we compute the sensitivity kernel using the adjoint-state method. This method avoids the computation of ray paths and makes the computational cost nearly independent of the number of receivers. We apply our new method in Thailand and adjacent regions. The final velocity model reveals a thick lithosphere beneath the Khorat Plateau and two mantle upwelling branches beneath its southern and western margins. The mantle upwelling may result from the mantle convection triggered by surrounding subduction systems and/or a slab window of the Indian Plate. The presence of the mantle upwelling corresponds to the source zone of the erupted Cenozoic basalts in the Khorat Plateau, indicating lithospheric modification beneath the plateau. The insightful tomographic result verifies our method and provides new perspectives on the structural heterogeneities and dynamics of the Indochina Block.

Plain Language Summary We propose a novel teleseismic traveltime tomography method based on the adjoint-state method. The critical procedure of computing sensitivity kernels is realized by solving the Eikonal and adjoint equations. This approach eliminates the need for calculating ray paths, which is required in conventional ray-based tomography methods. As a result, our approach avoids the potential failures of conventional shooting and bending methods for ray tracing and makes the computational cost independent of the number of receivers. We test our new method in Thailand, using the new data from the Thai Seismic Array. Our model reveals a thick lithosphere beneath the Khorat Plateau as a high-velocity anomaly. In addition, two mantle upwelling branches are imaged beneath the southern and western margins of the plateau as low-velocity anomalies. These anomalies are likely driven by surrounding subduction systems and may also be associated with the slab window of the Indian Plate. The presence of mantle upwelling aligns with the source zone of the exposed Cenozoic basalts and may suggest the lithospheric modification beneath the Khorat Plateau.

1. Introduction

Teleseismic traveltime tomography, which inverts differential arrival times of distant earthquakes, is a valuable tool for illuminating mantle structures beneath seismic arrays (Aki et al., 1977; Rawlinson et al., 2006; D. Zhao et al., 1994). Compared with local earthquake tomography, teleseismic traveltime tomography does not rely on local seismicity, broadening the scope of imaging to aseismic areas (Rawlinson & Fishwick, 2012). In addition, teleseismic waves travel through deep regions and crisscross beneath the seismic array, enabling the illumination of mantle structures (Liu et al., 2021; Yao et al., 2021). These advantages facilitate the wide applications of teleseismic traveltime tomography, which have contributed significantly to our understanding of the mantle structures and related dynamic processes (Aki et al., 1977; Benz et al., 1992; Bianchi et al., 2013; Lei & Zhao, 2016;

Liu et al., 2018; Oncescu et al., 1984; Rawlinson & Fishwick, 2012; Rawlinson & Kennett, 2008; Saltzer & Humphreys, 1997; Yao et al., 2021; D. Zhao et al., 1994).

A fundamental assumption in teleseismic traveltime tomography is that uncertainties in hypocentral parameters and structural heterogeneities outside the study region have negligible impacts on imaging receiver-side structures (Aki et al., 1977; Liu et al., 2018; Rawlinson et al., 2006; Steck et al., 1998). This is because generally common-source differential arrival times are used, and the wave paths from the source to adjacent receivers nearly overlap outside the study region (D. Zhao et al., 2013). This assumption allows for simulating wavefront propagation to be confined within the local domain. The wavefront propagation from the source to the boundary of the study region is usually computed approximately in an efficient manner, for example, based on the plane wave assumption (Aki et al., 1977; Steck & Prothero, 1991) or a global spherically symmetric reference model (Lei & Zhao, 2016; Rawlinson et al., 2006; D. Zhao et al., 1994). Initially, teleseismic traveltime tomography was conducted by tracing ray paths using fast but approximated approaches to predict traveltimes and compute sensitivity kernels (Aki et al., 1977; Steck et al., 1998; Weiland et al., 1995). More recently, the traveltime field of the first arrival can be accurately computed by solving Eikonal equations in complex media (Liu et al., 2018; Rawlinson et al., 2006, 2008), and accurate ray paths can be determined by tracing backward from the receivers to the local boundary along the negative gradient direction of the traveltime field. In addition to the traveltimes of first arrivals, waveform information can be extensively used in waveform-based teleseismic tomography (Beller et al., 2018; Monteiller et al., 2015; Wang et al., 2022), which improves the illumination of near-surface structures. However, this approach requires much more computational resources for wave propagation simulation.

We demonstrate that the computation of ray paths is avoidable in teleseismic traveltime tomography. We propose a novel framework for teleseismic traveltime tomography based on the adjoint-state method. Specifically, the tomographic inverse problem is formulated as an Eikonal equation-constrained optimization problem that minimizes the discrepancy between observational and predicted differential arrival times. The Fréchet derivative of the objective function with respect to the model parameter is computed by solving an adjoint equation instead of relying on ray paths. The independence of computing ray paths not only avoids the potential failures of conventional shooting and bending methods for ray tracing (Hole & Zelt, 1995; Rawlinson et al., 2008; Vidale, 1988) but also makes the computational cost nearly independent of the number of receivers. After that, model parameters are updated in an iterative fashion, in which the multi-grid model parameterization (Tong et al., 2019) and the step size-controlled gradient descent method (Tong, 2021a) are applied. Our new method is a significant extension of the adjoint-state traveltime tomography method (Tong, 2021a; Tong et al., 2024) to teleseismic traveltime tomography, which is then benchmarked in Thailand and adjacent regions using the new seismic data recorded by the Thai Seismic Array (TSAR) (S. Tanaka et al., 2019).

The paper is organized as follows. Section 2 develops the adjoint-state teleseismic traveltime tomography method. Its real-data application and benchmark in Thailand and adjacent regions are introduced in Section 3. Imaging results are presented in Section 4, followed by geological interpretation in Section 5. Finally, we conclude this paper in Section 6.

2. Adjoint-State Teleseismic Traveltime Tomography

2.1. Prediction of Teleseismic Traveltimes

We predict the traveltime field $T(\boldsymbol{x})$ from the source $\boldsymbol{x}_s$ outside the study region to any position $\boldsymbol{x}$ within the study region Ω in two steps. Here $\boldsymbol{x} = (r, \theta, \phi)$ denotes a position inside the Earth's volume, where r is the radius measuring the distance to the Earth's center, θ represents the latitude, and ϕ is the longitude. $\boldsymbol{x}_s = (r_s, \theta_s, \phi_s)$ is the source location.

First, we compute the traveltime from the source to the boundary (north, south, east, west, and bottom surfaces) of the study region. Under the assumption that heterogeneity outside the study region has a negligible impact on the imaging of receiver-side structures when inverting common-source differential arrival times (Aki et al., 1977; Liu et al., 2018; Rawlinson et al., 2006; Steck et al., 1998), we simply simulate the wavefront propagation from the source to the boundary of the study region in a spherically symmetric global reference model such as the AK135 model (Kennett et al., 1995). Due to the spherical symmetry, the traveltime $t(\boldsymbol{x}; \boldsymbol{x}_s)$ from the source $\boldsymbol{x}_s$ to any point $\boldsymbol{x}$ on the boundary $\Gamma \subset \partial\Omega$ depends on the radii at the two locations, that is, r and r_s, and the epicenter distance Ψ, expressed by

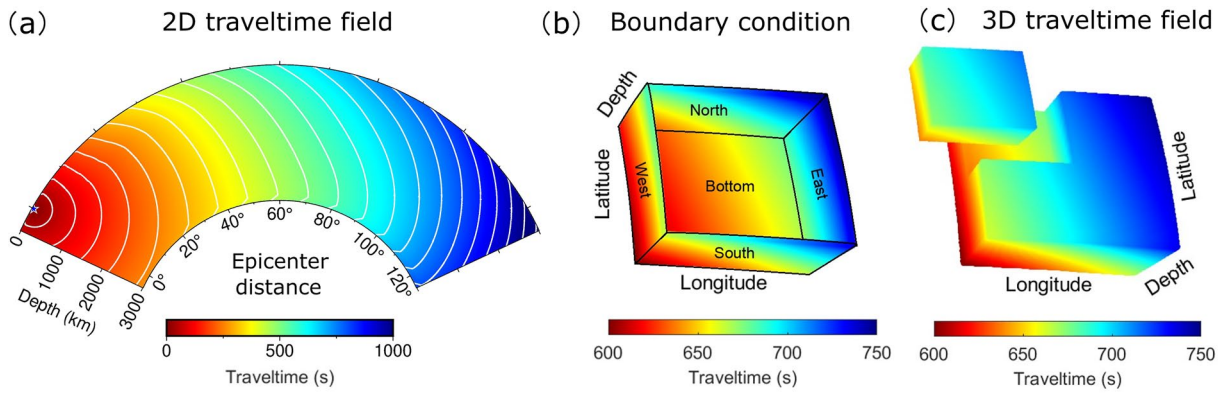

Figure 1. Illustration of teleseismic traveltime prediction. (a) The 2D traveltime field originating from the earthquake (blue star), which is obtained by solving the 2D Eikonal equation in the AK135 model (Kennett et al., 1995). White lines are traveltime isochrones at an interval of 50 s. (b) The traveltime field projected onto the north, south, east, west, and bottom surfaces of the study region based on the 2D traveltime field shown in panel (a). (c) The traveltime field in the 3D study region, which is obtained by solving the 3D Eikonal equation with the boundary conditions shown in panel (b).

$$t(\boldsymbol{x};\boldsymbol{x}_s) = \tau(r, \Psi(\theta,\phi;\theta_s,\phi_s); r_s), \tag{1}$$

where the epicenter distance Ψ has an analytic expression of

$$\Psi(\theta,\phi;\theta_s,\phi_s) = \arccos(\sin\theta\ \sin\theta_s + \cos\theta\cos\theta_s\cos(\phi-\phi_s)) + \epsilon(\theta,\phi;\theta_s,\phi_s). \tag{2}$$

Here $\epsilon(\theta, \phi; \theta_s, \phi_s)$ is a correction term for the Earth's ellipticity. The traveltime field $\tau(r, \psi; r_s)$ can be described by a 2D Eikonal equation in spherical coordinates

$$\begin{cases} \left\|\nabla\tau(r,\psi;r_s)\right\|^2 = s_{1D}^2(r), \quad (r,\psi)\in(0,R]\times[0,2\pi), \\ \tau(r_s,0;r_s) = 0, \end{cases} \tag{3}$$

where $\nabla\tau = \left(\partial_r\tau, \frac{1}{r}\partial_\psi\tau\right)$, and $s_{1D}(r)$ is the slowness (reciprocal of velocity) at radius r. Figures 1a and 1b illustrate an example of the 2D traveltime field $\tau(r, \psi; r_s)$ and the traveltime $t(\boldsymbol{x}; \boldsymbol{x}_s)$ from the source to the boundary Γ of a 3D region.

Second, we compute the traveltime field $T(\boldsymbol{x})$ in the local volume Ω (Figure 1c), which satisfies a 3D Eikonal equation with given boundary conditions

$$\begin{cases} \left\|\nabla T(\boldsymbol{x})\right\|^2 = s^2(\boldsymbol{x}), \quad \boldsymbol{x}\in\Omega, \\ T(\boldsymbol{x}) = t(\boldsymbol{x};\boldsymbol{x}_s), \quad \boldsymbol{x}\in\Gamma\subset\partial\Omega. \end{cases} \tag{4}$$

Here $\nabla T = \left(\partial_r T, \frac{1}{r}\partial_\theta T, \frac{1}{r\cos\theta}\partial_\phi T\right)$, and $s(\boldsymbol{x})$ represents the 3D slowness of the study region.

According to the above discussion, we can predict the traveltimes from a teleseismic event to any positions in the study region by solving a 2D and a 3D Eikonal equation. In this study, we employ the grid-based fast sweeping method to solve the Eikonal equations (Fomel et al., 2009; Luo & Qian, 2012; Tsai et al., 2003; H. Zhao, 2005). It is worth noting that the 2D Eikonal equation only needs to be solved once for each distant source to acquire the traveltimes to the local boundary, as the velocity model outside the study region remains unchanged during the inversion. In addition, solving the 2D Eikonal equation also enables us to consider structural heterogeneity outside of the 3D study region when computing the traveltime from the source to the local boundary, by replacing the 1D slowness model $s_{1D}(r)$ with a 2D slowness model $s_{2D}(r, \psi)$ in Equation 3.

2.2. The Fréchet Derivative

The main objective of teleseismic traveltime tomography is to determine an optimal slowness model $s(\boldsymbol{x})$ that minimizes the discrepancy between predicted and observational differential arrival times. A differential

arrival time (also called differential traveltime) is the difference between the traveltimes of two waves originating from the same earthquake but recorded by two separate stations, which can be accurately measured either manually or using a cross-correlation approach (Liu et al., 2019; Pan et al., 2022; Tong et al., 2024). We formulate teleseismic traveltime tomography as an Eikonal equation-constrained optimization problem, given by

$$\min_{s(\boldsymbol{x}),\hat{\boldsymbol{T}}} \chi\left(s(\boldsymbol{x}),\hat{\boldsymbol{T}}\right) \triangleq \sum_{n=1}^{N_s}\sum_{i=1}^{N_r}\sum_{j=1}^{N_r}\frac{w_{n,ij}}{2}\left(\Delta T_{n,ij}-\Delta T^{o}_{n,ij}+\hat{T}_i-\hat{T}_j\right)^2, \tag{5}$$

$$\text{subject to} \qquad \Delta T_{n,ij} = T_n(\boldsymbol{x}_{r,i}) - T_n(\boldsymbol{x}_{r,j}), \tag{6}$$

$$\begin{cases} \left\|\nabla T_n(\boldsymbol{x})\right\|^2 = s^2(\boldsymbol{x}), & \boldsymbol{x}\in\Omega, \\ T_n(\boldsymbol{x}) = t_n(\boldsymbol{x}), & \boldsymbol{x}\in\Gamma\subset\partial\Omega, \end{cases} \tag{7}$$

$$t_n(\boldsymbol{x}) = \tau_n(r,\Psi(\theta,\phi;\theta_{s,n},\phi_{s,n})), \tag{8}$$

$$\begin{cases} \left\|\nabla\tau_n(r,\psi)\right\|^2 = s^2_{1D}(r), & (r,\psi)\in(0,R]\times(0,2\pi], \\ \tau_n(r_{s,n},0) = 0. \end{cases} \tag{9}$$

Here $\Delta T_{n,ij} = T_n(\boldsymbol{x}_{r,i}) - T_n(\boldsymbol{x}_{r,j})$ is the predicted differential traveltime, in which $T_n(\boldsymbol{x}_{r,i})$ is the predicted traveltime of a wave originating from the n-th earthquake at $\boldsymbol{x}_{s,n} = (r_{s,n}, \theta_{s,n}, \phi_{s,n}), n = 1,\ldots,N_s$, and recorded by the i-th seismic station at $\boldsymbol{x}_{r,i} = (r_{r,i}, \theta_{r,i}, \phi_{r,i}), i = 1,\ldots,N_r$. Similarly, $\Delta T^{o}_{n,ij}$ denotes the observational differential traveltime, which can be extracted from the waveform data using the multi-channel cross-correlation (MCCC) technique (VanDecar & Crosson, 1990). The weight coefficient $w_{n,ij}$ reflects the existence and reliability of the differential traveltime data. We introduce additional unknowns $\hat{\boldsymbol{T}} = \left(\hat{T}_1,\ldots,\hat{T}_{N_r}\right)$ as the traveltime corrections associated with seismic stations (Frederiksen et al., 1998; Graeber et al., 2002). These station correction terms can absorb the traveltime residual contributed by the unresolvable shallow heterogeneities (Rawlinson et al., 2006).

We derive the Fréchet derivative of the objective function with respect to slowness $s(\boldsymbol{x})$ based on the adjoint-state method. For the sake of notation simplicity, we omit the dependence on $\boldsymbol{x}$ in the following derivation. A small model perturbation $\delta s(\boldsymbol{x})$ causes a small perturbation of the traveltime field $\delta T_n(\boldsymbol{x})$, satisfying

$$\begin{cases} \left\|\nabla T_n\right\|^2 + \left\|\nabla\delta T_n\right\|^2 + 2\nabla T_n\cdot\nabla\delta T_n = (s+\delta s)^2, & \boldsymbol{x}\in\Omega, \\ T_n(\boldsymbol{x}) + \delta T_n(\boldsymbol{x}) = t_n(\boldsymbol{x}), & \boldsymbol{x}\in\Gamma\subset\partial\Omega. \end{cases} \tag{10}$$

Subtracting Equation 7 from Equation 10 and ignoring second and higher-order terms yield

$$\begin{cases} \nabla T_n\cdot\nabla\delta T_n = s\delta s, & \boldsymbol{x}\in\Omega, \\ \delta T_n(\boldsymbol{x}) = 0, & \boldsymbol{x}\in\Gamma\subset\partial\Omega. \end{cases} \tag{11}$$

We multiply a test function $P_n(\boldsymbol{x})$ on both sides of Equation 11 and integrate over the volume Ω

$$\int_\Omega P_n\nabla T_n\cdot\nabla\delta T_n \mathrm{d}\boldsymbol{x} = \int_\Omega P_n s\delta s \mathrm{d}\boldsymbol{x}. \tag{12}$$

Using integration by parts and the Gauss theorem, we have

$$\int_{\partial\Omega}\boldsymbol{n}\cdot(P_n\nabla T_n\cdot\delta T_n)\mathrm{d}\sigma + \int_\Omega \delta T_n\nabla\cdot(P_n(-\nabla T_n))\mathrm{d}\boldsymbol{x} = \int_\Omega P_n s\delta s\mathrm{d}\boldsymbol{x}, \tag{13}$$

where $\boldsymbol{n}$ is the outer unit normal of $\partial\Omega$. If $P_n(\boldsymbol{x})$ satisfies the adjoint equation

$$\begin{cases} \nabla \cdot (P_n(-\nabla T_n)) = 2\sum_{i=1}^{N_r}\left(\sum_{j=1}^{N_r} w_{n,ij}\left(\Delta T_{n,ij} - \Delta T^o_{n,ij} + \hat{T}_i - \hat{T}_j\right)\right)\delta(\boldsymbol{x} - \boldsymbol{x}_{r,i}), \quad \boldsymbol{x} \in \Omega, \\ P_n(\boldsymbol{x}) = 0, \quad \boldsymbol{x} \in \partial\Omega\backslash\Gamma, \end{cases} \tag{14}$$

then a linear relationship between the slowness perturbation $\delta s(\boldsymbol{x})$ and the perturbation of the objective function $\delta\chi$ can be established by ignoring second and higher-order terms,

$$\begin{aligned} \delta\chi &= \sum_{n=1}^{N_s}\sum_{i=1}^{N_r}\sum_{j=1}^{N_r} w_{n,ij}\left(\Delta T_{n,ij} - \Delta T^o_{n,ij} + \hat{T}_i - \hat{T}_j\right)(\delta T_n(\boldsymbol{x}_{r,i}) - \delta T_n(\boldsymbol{x}_{r,j})) \\ &= \sum_{n=1}^{N_s}\int_\Omega \sum_{i=1}^{N_r}\sum_{j=1}^{N_r} w_{n,ij}\left(\Delta T_{n,ij} - \Delta T^o_{n,ij} + \hat{T}_i - \hat{T}_j\right)\delta T_n(\boldsymbol{x})(\delta(\boldsymbol{x} - \boldsymbol{x}_{r,i}) - \delta(\boldsymbol{x} - \boldsymbol{x}_{r,j}))\mathrm{d}\boldsymbol{x} \\ &= \sum_{n=1}^{N_s}\int_\Omega \delta T_n(\boldsymbol{x}) 2\sum_{i=1}^{N_r}\left(\sum_{j=1}^{N_r} w_{n,ij}\left(\Delta T_{n,ij} - \Delta T^o_{n,ij} + \hat{T}_i - \hat{T}_j\right)\right)\delta(\boldsymbol{x} - \boldsymbol{x}_{r,i})\mathrm{d}\boldsymbol{x} \\ &= \sum_{n=1}^{N_s}\int_\Omega \delta T_n \nabla \cdot (P_n(-\nabla T_n))\mathrm{d}\boldsymbol{x} = \sum_{n=1}^{N_s}\int_\Omega P_n s \delta s \mathrm{d}\boldsymbol{x}. \end{aligned} \tag{15}$$

The above equation derives the Fréchet derivative of the objective function with respect to slowness, which is also called sensitivity kernel,

$$\delta\chi = \int_\Omega K_s(\boldsymbol{x})\frac{\delta s(\boldsymbol{x})}{s(\boldsymbol{x})}\mathrm{d}\boldsymbol{x}, \quad K_s(\boldsymbol{x}) = \sum_{n=1}^{N_s} P_n(\boldsymbol{x}) s^2(\boldsymbol{x}). \tag{16}$$

It is more straightforward to derive the sensitivity kernel with respect to station correction term $\hat{\boldsymbol{T}}$, given by

$$K_{\hat{T}_i} = 2\sum_{n=1}^{N_s}\sum_{j=1}^{N_r} w_{n,ij}\left(\Delta T_{n,ij} - \Delta T^o_{n,ij} + \hat{T}_i - \hat{T}_j\right), \quad i = 1, 2, \ldots, N_r. \tag{17}$$

The adjoint-state method enables the computation of sensitivity kernels by solving one adjoint equation for each source instead of computing ray paths for all source-receiver pairs. The adjoint Equation 14 describes the transportation of differential traveltime residuals backward from the receivers to the source along the negative gradient direction of the traveltime field. Since the actual source is outside the study region, the residuals are transported to the north, south, east, west, and/or bottom surface. Thus, the adjoint field is fixed as 0 only on the top surface, which differs from that in the adjoint-state traveltime tomography method for local earthquakes (Tong, 2021a). We employ the modified fast sweeping method (Leung & Qian, 2006) to solve the adjoint equation.

2.3. Model Parameterization and Optimization Algorithm

The adjoint-state method computes the sensitivity kernel with respect to slowness on the forward modeling grid. However, directly discretizing model perturbations on the forward modeling grid is unsuitable. Because the grid spacing, which is required to be sufficiently fine to guarantee the accuracy of traveltime prediction, may exceed the resolving ability of seismic data. To address this problem, we adopt the multi-grid model parameterization (Tong et al., 2019) to discretize model perturbations.

We design H sets of inversion grids and denote the l-th node of the h-th grid by

$$\boldsymbol{x}^h_l = \left(r^h_i, \theta^h_j, \phi^h_k\right), \quad h = 1, \cdots, H, \quad i = 1, \cdots, N^h_I, \tag{18}$$

$$j = 1, \cdots, N^h_J, \quad k = 1, \cdots, N^h_K, \quad l = (k-1)N^h_I N^h_J + (j-1)N^h_I + i. \tag{19}$$

Every inversion grid should cover the study region

$$\Omega \subset \left[r^h_1, r^h_{N^h_I}\right] \times \left[\theta^h_1, \theta^h_{N^h_J}\right] \times \left[\phi^h_1, \phi^h_{N^h_K}\right], \quad h = 1, \ldots, H. \tag{20}$$

Each grid node is associated with a basis function

$$B_l^h(\boldsymbol{x}) = u_i^h(r)v_j^h(\theta)w_k^h(\phi), \quad 1 \le l \le L^h = N_I^h N_J^h N_K^h, \tag{21}$$

where

$$u_i^h(r) = \begin{cases} \frac{r - r_{i-1}^h}{r_i^h - r_{i-1}^h}, & \text{if } r_{i-1}^h \le r \le r_i^h, \\ \frac{r_{i+1}^h - r}{r_{i+1}^h - r_i^h}, & \text{if } r_i^h < r \le r_{i+1}^h, \\ 0, & \text{otherwise,} \end{cases} \quad v_j^h(\theta) = \begin{cases} \frac{\theta - \theta_{j-1}^h}{\theta_j^h - \theta_{j-1}^h}, & \text{if } \theta_{j-1}^h \le \theta \le \theta_j^h, \\ \frac{\theta_{j+1}^h - \theta}{\theta_{j+1}^h - \theta_j^h}, & \text{if } \theta_j^h < \theta \le \theta_{j+1}^h, \\ 0, & \text{otherwise,} \end{cases}$$
$$w_k^h(\phi) = \begin{cases} \frac{\phi - \phi_{k-1}^h}{\phi_k^h - \phi_{k-1}^h}, & \text{if } \phi_{k-1}^h \le \phi \le \phi_k^h, \\ \frac{\phi_{k+1}^h - \phi}{\phi_{k+1}^h - \phi_k^h}, & \text{if } \phi_k^h < \phi \le \phi_{k+1}^h. \\ 0, & \text{otherwise.} \end{cases} \tag{22}$$

Here $r_0^h, \theta_0^h, \phi_0^h$ and $r_{N_I^h+1}^h, \theta_{N_J^h+1}^h, \phi_{N_K^h+1}^h$ can be specified as

$$\begin{aligned} r_0^h &= 2r_1^h - r_2^h, & \theta_0^h &= 2\theta_1^h - \theta_2^h, & \phi_0^h &= 2\phi_1^h - \phi_2^h, \\ r_{N_I^h+1}^h &= 2r_{N_I^h}^h - r_{N_I^h-1}^h, & \theta_{N_J^h+1}^h &= 2\theta_{N_J^h}^h - \theta_{N_J^h-1}^h, & \phi_{N_K^h+1}^h &= 2\phi_{N_K^h}^h - \phi_{N_K^h-1}^h. \end{aligned} \tag{23}$$

The model perturbation is assumed to be smooth and can be approximated as a linear combination of the basis functions related to a specific inversion grid. If we further average the perturbation models across all inversion grids, then the model perturbation can be formulated as

$$\frac{\delta s(\boldsymbol{x})}{s(\boldsymbol{x})} = \frac{1}{H}\sum_{h=1}^{H}\sum_{l=1}^{N_L}\delta C_l^h B_l^h(\boldsymbol{x}). \tag{24}$$

Plugging the above equation into Equation 16, we derive the sensitivity kernel of the objective function with respect to the auxiliary parameters C_l^h

$$\delta\chi = \sum_{h=1}^{H}\sum_{l=1}^{N_L} K_l^h \delta C_l^h, \quad K_l^h = \frac{1}{H}\int_\Omega K_s(\boldsymbol{x})B_l^h(\boldsymbol{x})\mathrm{d}\boldsymbol{x}. \tag{25}$$

This method simplifies the optimization problem in an infinite-dimensional function space into a problem in a finite-dimensional vector space, thus significantly reducing the number of unknowns. Additionally, averaging the perturbation models across multiple inversion grids mitigates the potential error caused by the subjective selection of a single inversion grid, which improves the robustness of the inversion and the reliability of the result.

We employ the step size-controlled gradient descent method to iteratively update the slowness and station correction terms (Tong, 2021a). The perturbations in the relative slowness and station correction terms are along the negative gradient direction, but their amplitudes are limited to less than 1% and 0.01 s at each iteration, respectively. Note that the upper bounds for the perturbations decrease once the objective function increases, ensuring the convergence of iteration (J. Chen et al., 2023). In all, this restriction is similar to adding a damping parameter, which has been verified by previous studies (J. Chen et al., 2023; Liu et al., 2019; Tong, 2021a, 2021b).

3. Application: Tomography of Thailand and Adjacent Regions

3.1. Tectonic Background

The Indochina Peninsula, which sits above the mantle wedge of the subducting Indian Plate beneath the Eurasian and Sunda Plates (Y. Yu et al., 2017), is the largest landmass in Southeast Asia (Figure 2). This peninsula comprises two main blocks: the Shan-Thai Block in the northwest and the Indochina Block in the southeast, separated by the NE-SW trending Dien Bien Phu Fault. The Shan-Thai Block is bounded by the Sagaing Fault in the west and is separated from the South China Block (SCB) by the NW-SE trending Ailao Shan-Red River Fault

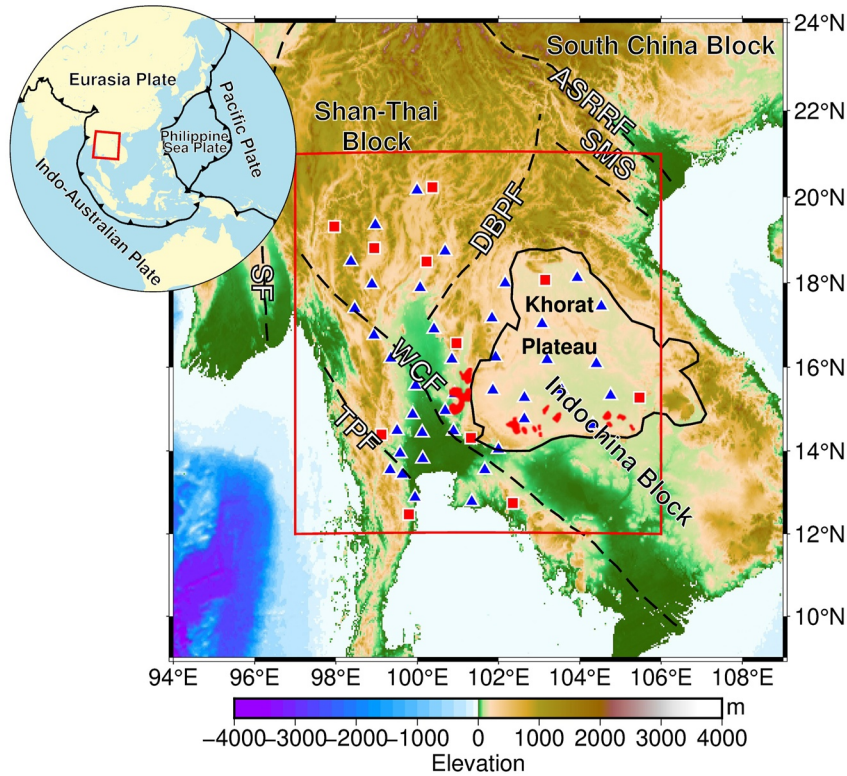

Figure 2. The topographic map of the Indochina Peninsula. The black dashed lines represent major faults and sutures. SF, Sagaing Fault; TPF, Three Pagodas Fault; WCF, Wang-Chao Fault; DBPF, Dien Bien Phu Fault; ASRRF, Ailao Shan-Red River Fault; and SMS, Song Ma Suture. The black line denotes the boundary of the Khorat Plateau. The study region is within the red box. The blue triangles are seismic stations from the TSAR. The red squares denote additional permanent stations. The exposed basalts within the study region are shown in red. The surrounding subduction systems of the Indo-Australian, Pacific, and Philippine Sea Plates are labeled in the top left subfigure.

(ASRRF). The Indochina Block is also separated from the SCB by ASRRF in the north. Its southwestern edge is demarcated by the Wang Chao Fault and the Three Pagodas Fault (Singsoupho et al., 2014).

The collision between the Indian and Eurasian Plates since the early Eocene (Huchon et al., 1994; Tapponnier et al., 1982) has led to a southeastward displacement and clockwise rotation of the Shan-Thai Block and the Indochina Block along the ASRRF (Takemoto et al., 2009; K. Tanaka et al., 2008). This process has induced strong internal deformation in the Shan-Thai Block. In contrast, the Khorat Plateau, as the core of the Indochina Block, behaves like a rigid block with little internal deformation (K. Tanaka et al., 2008). Some studies (Takemoto et al., 2009; Yang et al., 2015) attribute this contrast to a thick lithosphere beneath the plateau that is imaged in numerous studies (H. Chen et al., 2021; Lebedev & Nolet, 2003; Li & van der Hilst, 2010; Li et al., 2006; Yang et al., 2015; C. Yu et al., 2017). However, the thick lithosphere with little internal deformation cannot explain the Cenozoic basalts originating from the mantle that is exposed in the southern and western margins of the Khorat Plateau (Yan et al., 2018; Zhou & Mukasa, 1997). To investigate the origin of the exposed basalts and to improve our understanding of the geological dynamics in the Indochina Peninsula, we take advantage of the recently deployed TSAR (S. Tanaka et al., 2019) and perform the adjoint-state teleseismic traveltime tomography to obtain a refined seismic velocity model beneath the Khorat Plateau and adjacent regions.

3.2. Study Region and Seismic Data

Our study region is located in the central Indochina Peninsula, ranging from 97° to 106°E and from 12° to 21°N. The used teleseismic data were mainly recorded by 40 broadband seismic stations from the TSAR network operated from January 2017 to December 2018 (S. Tanaka et al., 2019). These stations are uniformly distributed in Thailand with an average station spacing of approximately 100 km (blue triangles in Figure 2). To improve the

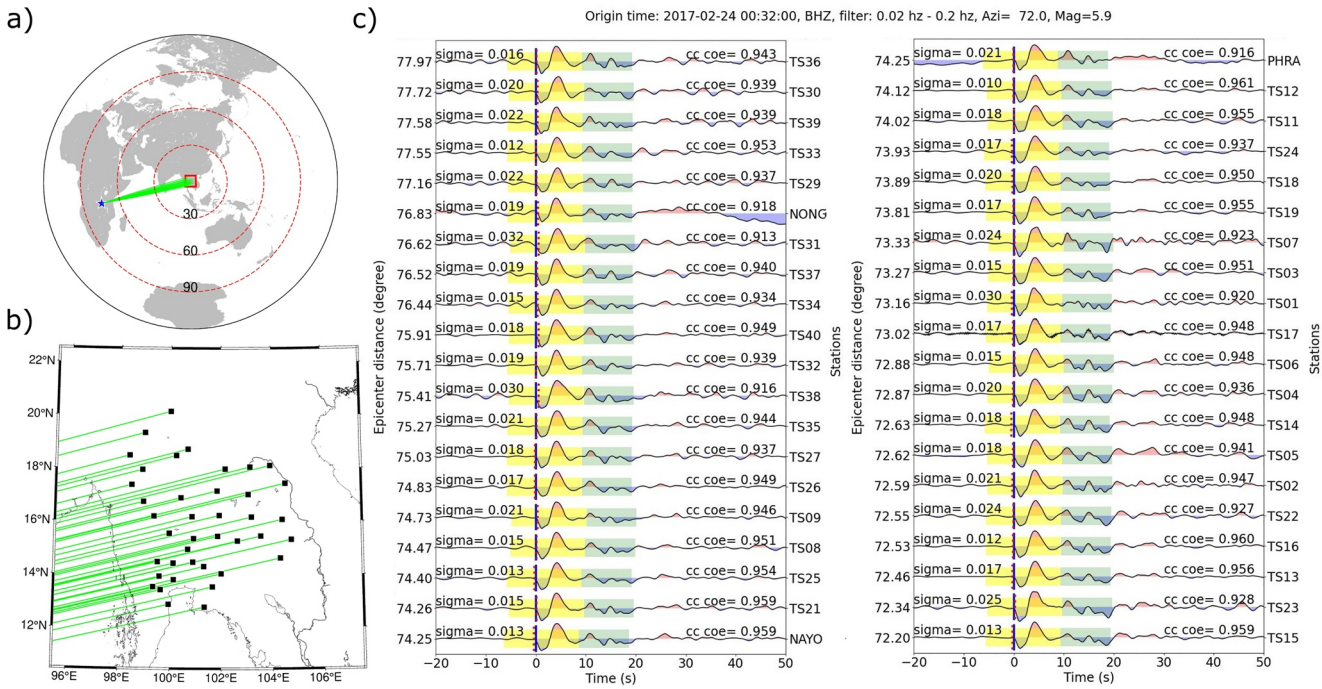

Figure 3. An example of differential traveltime measurement using the multi-channel cross-correlation (MCCC) technique. (a) Event location map. The blue star is the earthquake. The study region is within the red box. The dashed circles denote epicenter distances of 30°, 60°, and 90°. (b) The great-circle paths (green lines) of the teleseismic traveltime data from the earthquake to the seismic stations (black squares). (c) The event waveforms aligned with the computed arrival time (blue line) using MCCC. The red dotted lines are the theoretical arrival times computed in the AK135 global reference model (Kennett et al., 1995). Multiple time windows are used to determine the optimal cross-correlation differential traveltime. These time windows have varying lengths from 15 to 25 s, which begin at the left boundary of the yellow-shaded interval and end within the green-shaded interval. "sigma" denotes the standard deviation of residuals in second, and "cc coe" means the average value of the cross-correlation coefficients related to other waveforms.

station coverage, we also utilize the data recorded by 11 permanent stations in the same period (red squares in Figure 2).

We select teleseismic earthquakes with epicenter distances between 30° and 90° and magnitudes greater than 5.0. Raw seismograms are processed by deconvolving the instrument response and applying a bandpass filter of 0.02–0.2 Hz. Then, the MCCC technique is employed to accurately measure the differential traveltimes of first P-arrivals (VanDecar & Crosson, 1990). To avoid subjective selection of cross-correlation time window, we test 11 time windows, beginning at 5 s before the theoretical arrival time computed in the AK135 model (Kennett & Engdahl, 1991) and having varying lengths ranging from 15 to 25 s with a gap of 1 s. The differential traveltime is chosen based on the highest cross-correlation coefficient among all time windows (see an example in Figure 3).

We apply strict data selection criteria to refine the differential traveltime data. First, we only retain the waveforms with a signal-to-noise ratio (SNR) greater than 2.0, where the SNR is the ratio of the average amplitude in the signal window (from 0 to 15 s with respect to the theoretical arrival time) to that in the noise window (from −15 to 0 s). Second, we discard signals with a standard deviation of residuals greater than 1 s or an average cross-correlation coefficient less than 0.7 in MCCC. These two criteria are commonly used to elevate the quality of the signals and the associated differential traveltimes (VanDecar & Crosson, 1990). Third, we limit the inter-station distance to less than 2.5°, aiming at enhancing the overlapping of the wave paths outside the study region. This limitation can mitigate the influence of outside anomalies on the differential traveltimes (Liu et al., 2018, 2019; Yao et al., 2021). In addition, to reduce earthquake clustering, we divide the global region into subdomains with a spacing of 5° in azimuth, 5° in epicenter distance, and 100 km in depth. The top three earthquakes in terms of the number of reliable records are selected in each subdomain. The differential traveltime data of the unselected earthquakes are used to verify the final model (see data coverage in Figure S1 in Supporting Information S1). In total, we obtain 15,205 reliable differential traveltimes from 190 teleseismic earthquakes for the inversion (Figure 4). These data densely cover the study region, particularly the Khorat Plateau.

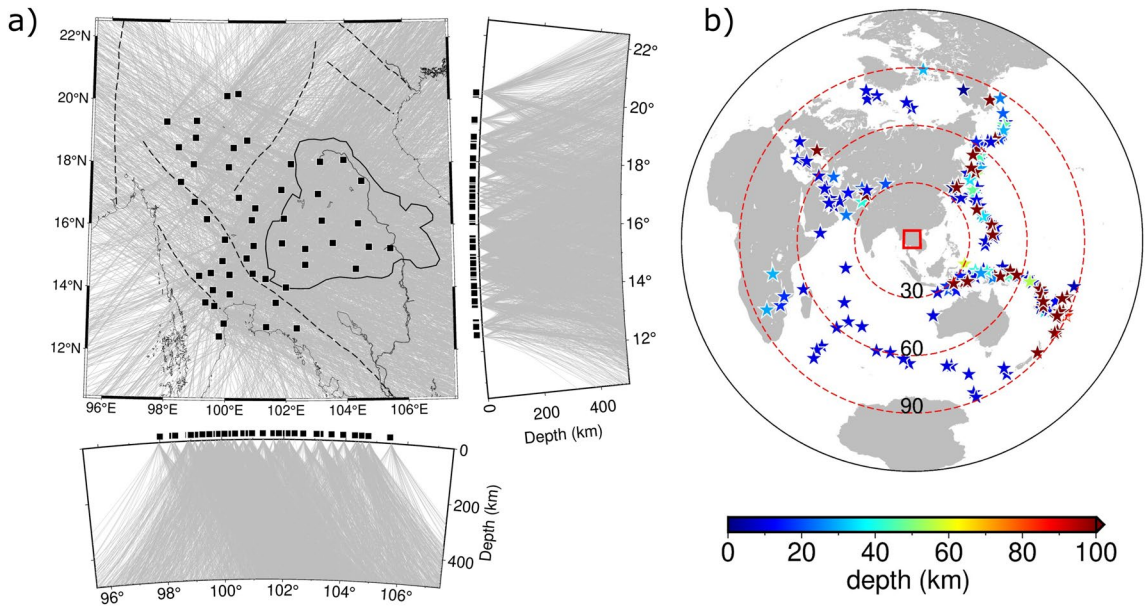

Figure 4. (a) The distribution of seismic stations (black squares) and great-circle paths associated with the teleseismic traveltime data for inversion. Major faults and sutures are denoted by black dashed lines. The black lines denote the boundary of the Khorat Plateau. (b) The distribution of the teleseismic earthquakes used for inversion. The study region is within the red box. The dashed circles denote epicenter distances of 30°, 60°, and 90°.

3.3. Checkerboard Resolution Test

We perform a checkerboard resolution test to assess the resolving ability of the selected differential traveltime data. The initial model (Figure S2 in Supporting Information S1) is constructed by adopting the Crust1.0 model (Laske et al., 2013) for the crustal *P*-wave velocity and setting the mantle *P*-wave velocity based on the global reference AK135 model (Kennett et al., 1995). The checkerboard model is constructed by assigning positive and negative velocity perturbations to the initial model in a staggered manner (Figure S3 in Supporting Information S1), which is expressed by

$$\frac{\Delta v(\boldsymbol{x})}{v(\boldsymbol{x})} = \begin{cases} 4\% \cdot \sin\left(\frac{\phi - 97^\circ}{3^\circ} \cdot 2\pi\right) \sin\left(\frac{\theta - 12^\circ}{3^\circ} \cdot 2\pi\right) \sin\left(\frac{z}{200} \cdot 2\pi\right), & 0\,\text{km} \le z \le 200\,\text{km}, \\ 3\% \cdot \sin\left(\frac{\phi - 97^\circ}{3^\circ} \cdot 2\pi\right) \sin\left(\frac{\theta - 12^\circ}{3^\circ} \cdot 2\pi\right) \sin\left(\frac{z - 200}{300} \cdot 2\pi\right), & 200\,\text{km} \le z \le 350\,\text{km}, \\ 2\% \cdot \sin\left(\frac{\phi - 97^\circ}{3^\circ} \cdot 2\pi\right) \sin\left(\frac{\theta - 12^\circ}{3^\circ} \cdot 2\pi\right) \sin\left(\frac{z - 200}{300} \cdot 2\pi\right), & 350\,\text{km} \le z \le 500\,\text{km}. \end{cases} \quad (26)$$

The observational differential traveltimes are computed numerically in the checkerboard model. To mimic the data noise, we assign Gaussian noise with mean 0 s and standard deviation 0.1 s to the computed differential traveltimes (Figure S4a in Supporting Information S1). We begin the inversion with the initial model and keep the same source-receiver configuration as that of the real data.

Examples of individual, event, and misfit kernels are shown in Figure 5, in which the misfit kernel exhibits consistency with the pattern of checkerboard velocity anomalies. A total of five inversion grids are positioned in a staggered way along the diagonal direction (Figure S5 in Supporting Information S1). To prevent spatial aliasing, we ensure that every wavelength anomaly is approximately sampled by five nodes of each inversion grid (Tong, 2021a). After 40 iterations, the standard deviation of differential traveltime residuals decreases from 0.241 to 0.112 s, which is close to the noise level (Figures S4b and S4c in Supporting Information S1). The results show that the alternating pattern of the velocity anomalies is well recovered beneath the region covered by the seismic network (within the gray box in Figure 6), which suggests that the selected data can reveal the subsurface velocity heterogeneity in our study region.

4. Tomographic Results and Restoration Resolution Tests

We follow the same inversion procedures as the checkerboard resolution test but use real differential traveltime data to image the subsurface velocity structures. After 40 iterations, the standard deviation of the differential

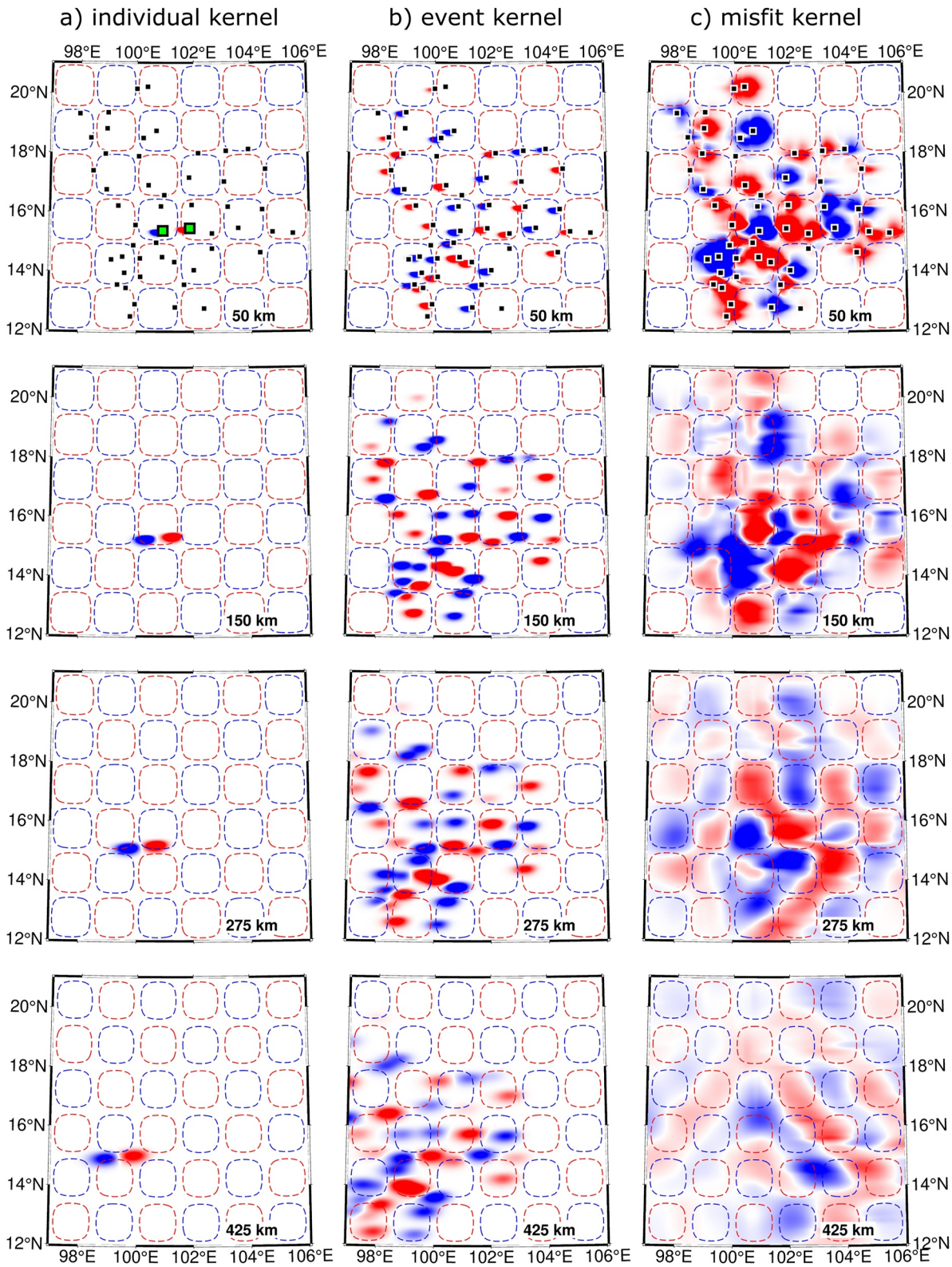

Figure 5. Horizontal sections of the sensitivity kernels computed in the initial model for the checkerboard resolution test. (a) The individual kernel corresponding to the earthquake shown in Figure 3 and a pair of stations (green squares). (b) The event kernel corresponding to the same earthquake and all station pairs. (c) The misfit kernel corresponding to all teleseismic earthquakes and station pairs. The black squares, shown at the section of 50 km depth, are seismic stations. The blue and red dashed boxes outline the positive and negative velocity perturbations of the checkerboard model, respectively.

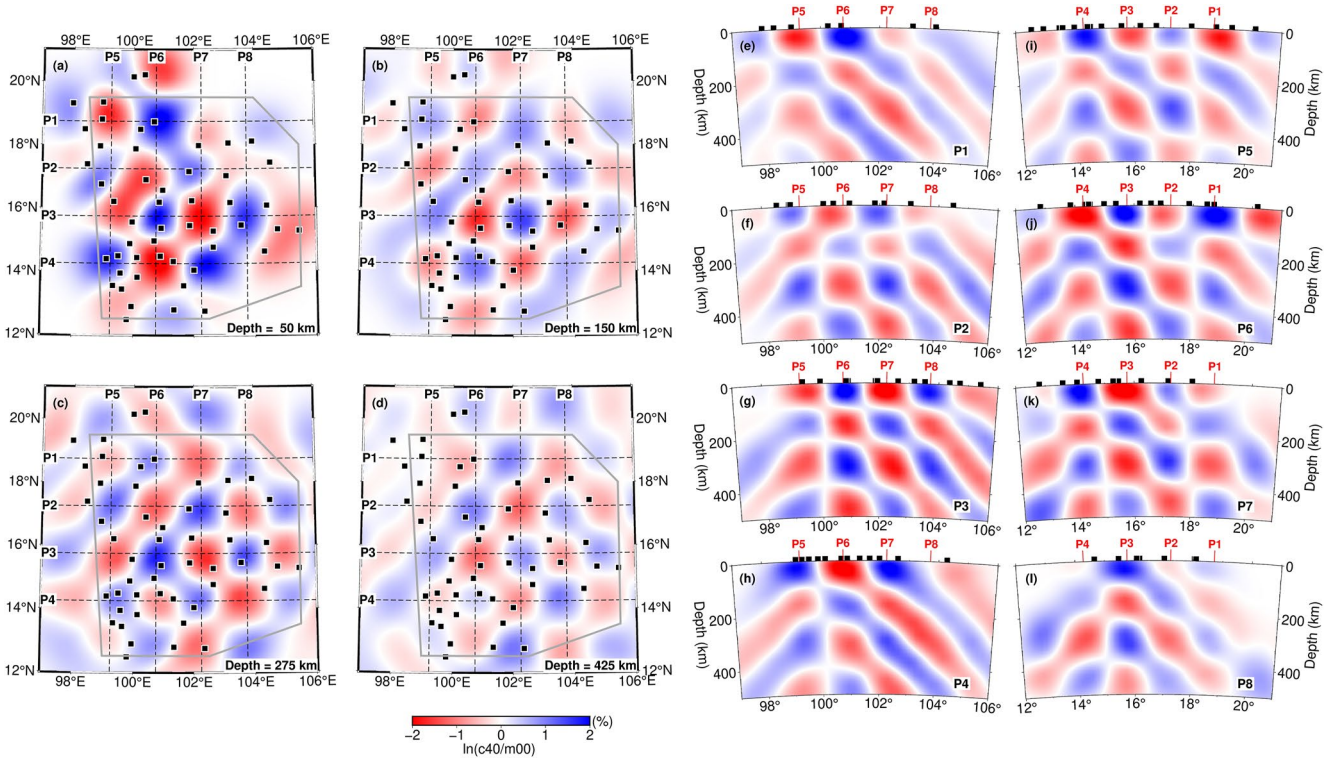

Figure 6. Horizontal and vertical sections of the inversion result of the checkerboard resolution test. (a) Horizontal sections at different depths. Regions within the gray box are considered resolvable. The black dashed lines mark the locations of the vertical sections. The black squares denote seismic stations. (b) The vertical sections crossing the center of checkerboard anomalies. The red vertical lines on the top denote the locations of other vertical profiles. The black squares represent the seismic stations within 0.75° along the profile.

traveltime residuals reduces from 0.370 to 0.177 s (Figures S6a and S6b in Supporting Information S1). Though the verification data (Figure S1 in Supporting Information S1) are not inverted, the standard deviation of their residuals also decreases from 0.380 to 0.231 s (Figure S6c in Supporting Information S1), suggesting the robustness of the final model.

The imaging results reveal several significant velocity anomalies in the study region. First, a broad high-velocity anomaly, labeled as H1, has been identified beneath the Khorat Plateau at depths of 50–250 km (Figures 7a–7e), which is gradually replaced by a low-velocity anomaly labeled as L3 at greater depths (Figures 7f–7h, 8a, and 8c). Second, a low-velocity anomaly (L1) is observed adjacent to the western margin of the Khorat Plateau, extending to a depth of 350 km (Figures 7a–7g, 8a, and 8b). Third, an eastward dipping low-velocity anomaly labeled as L2 is imaged in the southern margin of the Khorat Plateau. Its shallow part above 200 km depth is located at the southwestern corner of the plateau and is connected with L1 (Figures 7a–7d). As depth increases, the deep part of L2 below 200 km depth extends eastward and is separated from L1 (Figures 7e–7h and 8b). The locations of L1 and L2 coincide with the presence of exposed Cenozoic basalts in the western and southern margins of the Khorat Plateau. It is worth noting that the high- and low-velocity anomalies in our model should be regarded as positive and negative velocity perturbations relative to other parts of the model since only the differential traveltimes are inverted.

Teleseismic waves propagate upward to seismic stations on the surface, potentially causing vertical smearing in the imaging results. To verify the reliability of the labeled velocity anomalies, we perform a restoration resolution test, in which the target model is built by incorporating the labeled velocity anomalies H1, L1, L2, and L3. The result suggests that all the labeled anomalies can be successfully recovered (Figure 9). In the horizontal sections (Figures 9a–9h), the recovered velocity anomalies are in good agreement with the target model thanks to the dense station spacing. However, we can observe the smearing of the high-velocity anomaly H1 in a downward direction (Figures 9i and 9l), which seems to resemble the downward extension of H1 in the real-data imaging results (Figures 8a and 8d). The presence of H1 in our imaging result is consistent with previous studies (Li

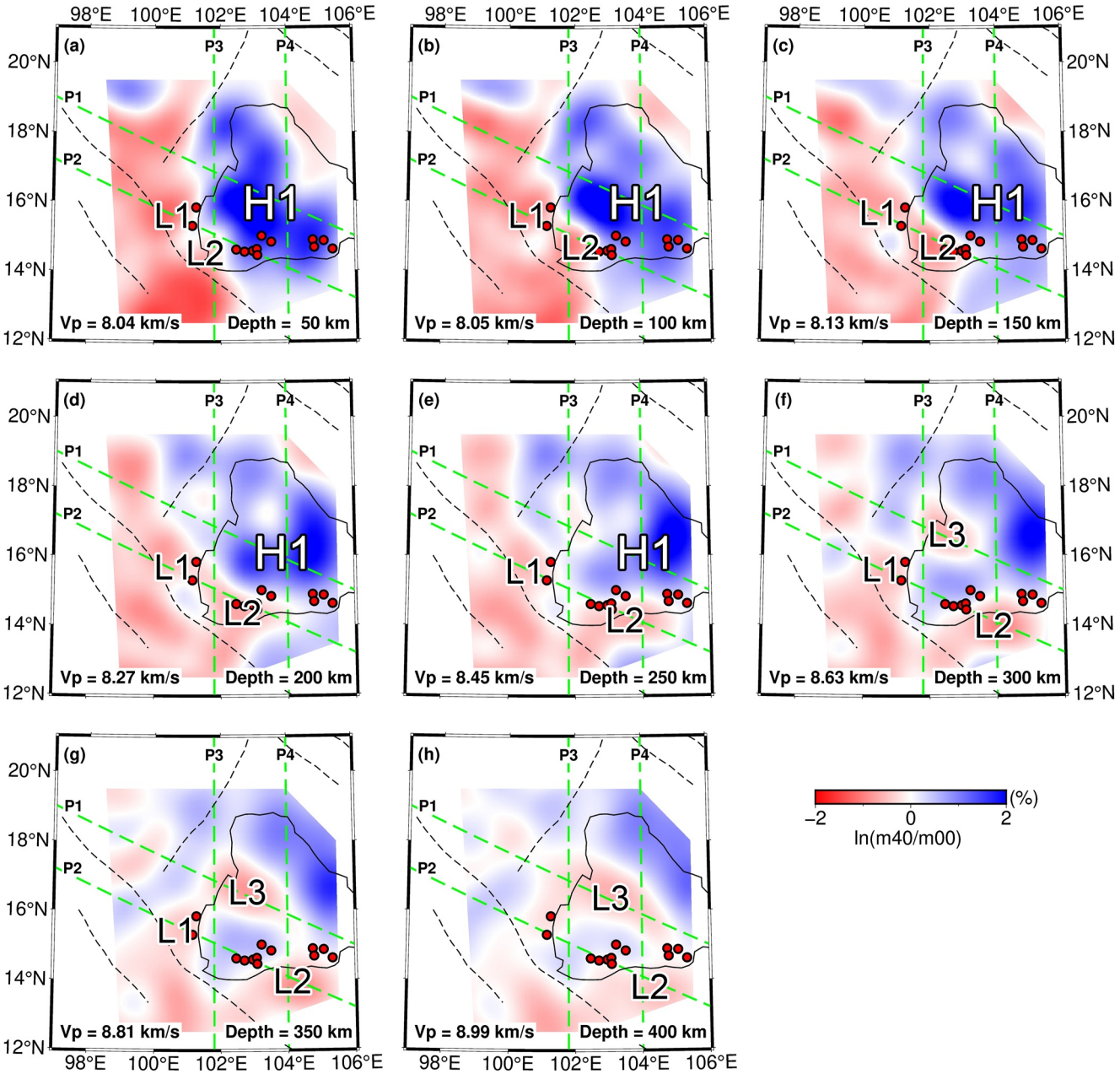

Figure 7. Horizontal sections of the imaging results. The images outside the station coverage are clipped out according to the gray box in Figure 6. Major faults and sutures are denoted by black dashed lines. The black lines denote the boundary of the Khorat Plateau. The green dashed lines are the locations of vertical sections in Figure 8. The red dots are the locations of exposed Cenozoic basalts.

et al., 2006; Yang et al., 2015). However, its thickness, which is suggested to be 150–200 km in previous studies, is not well constrained in our images due to the poor vertical resolving ability of the upward propagating waves.

The smearing of H1 in the restoration test indicates that all the anomalies in Figure 9 may have been distorted in the downward direction. Therefore, we conduct two additional restoration resolution tests to assess the reliability of L1 and L2. In the second test, only H1 and the sections above 200 km depth of L1 and L2 are preserved in the target model. The results show partial downward smearing of L1 and L2, but the amplitudes decrease significantly as depth increases beyond 200 km depth (Figures S7i and S7j in Supporting Information S1). This phenomenon differs from the real-data inversion (Figures 8a and 8b) and the first restoration test (Figures 9i and 9j), where the amplitudes of L1 and L2 at depths below 200 km are as strong as those of the shallow parts.

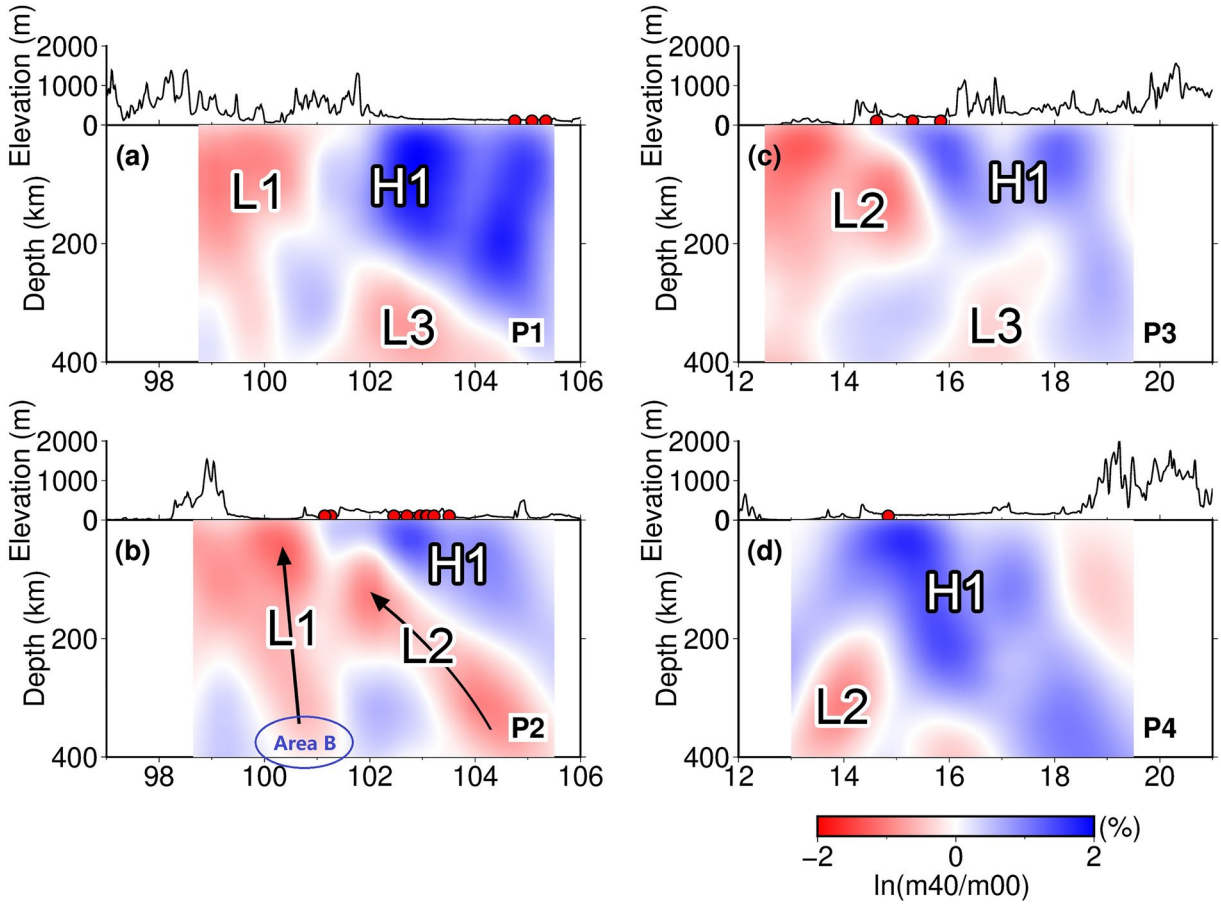

Figure 8. Vertical sections of the imaging result. The images outside the station coverage are clipped out. In panel (b), the black arrows represent the mantle upwelling, and the blue circle denotes the location of the thin mantle transition zone in Y. Yu et al. (2017), where a possible slab window is observed (Pesicek et al., 2008). The notations for other features within a distance of 0.75° along each profile are the same as those shown in Figure 7.

Thus, the deep parts of L1 and L2 are likely reliably resolved rather than artifacts caused by smearing. However, due to the relatively poor data coverage in the west, north, and south directions, it remains unclear whether the deep and shallow parts of L2 are connected or not. In the third test, we further exclude the shallow part of L2 from the target model of the second test. The purpose of this test is to verify the reliability of the shallow part of L2, the low-velocity anomaly in the southwestern corner of the Khorat Plateau above 200 km depth. The absence of L2 in the inverted model (Figures S8a–S8d, S8i, and S8j in Supporting Information S1) confirms its reliability.

5. Discussion

Tectonic activities in the Indochina Block have been primarily shaped by the collision of the Indian and Eurasian Plates since the early Eocene, resulting in substantial southeast extrusion and a clockwise rotation of the block (Huchon et al., 1994; Takemoto et al., 2009; Tapponnier et al., 1982). However, some evidence, such as the undeformed Mesozoic sediments covering a large portion of the Khorat Plateau (Richter & Fuller, 1996) and paleomagnetic studies (Sato et al., 2007; Takemoto et al., 2009; K. Tanaka et al., 2008), suggest that the Khorat Plateau has experienced much less internal deformation than the Shan-Thai block. The reason may be attributed to a cold and thick lithosphere beneath the plateau, imaged as a high-velocity anomaly (H1) in our tomographic result. The presence of this anomaly agrees with previous tomographic observations (H. Chen et al., 2021; Lebedev & Nolet, 2003; Li & van der Hilst, 2010; Li et al., 2006; Yang et al., 2015). According to the thermal structure inferred from *S*-wave velocity (C. Yu et al., 2017), this thick lithosphere is about 100°C colder than surrounding regions, making it more viscous (Lee et al., 2011) and thus less susceptible to internal deformation (Yang et al., 2015).

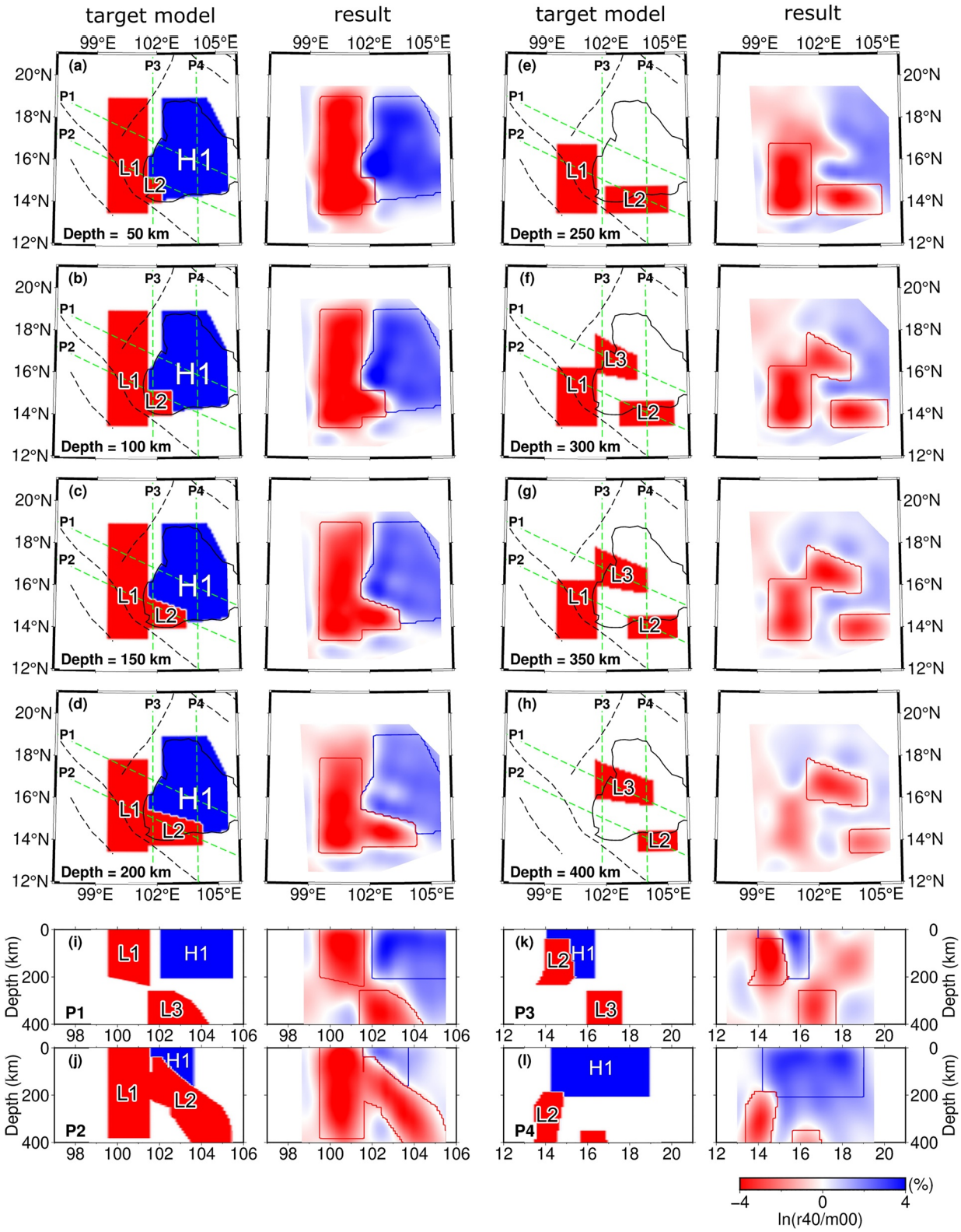

Figure 9. The horizontal and vertical sections of the target model and the inversion result of the first restoration resolution test. All labeled anomalies in Figure 7 are included in the target model. The notations and profile locations are identical to those in Figures 7 and 8.

Although the Khorat Plateau behaves like a rigid block, the presence of late Cenozoic volcanic activities along the southern and western margins of the Khorat Plateau may indicate lithospheric modifications beneath the plateau (Wu et al., 2022). The trace element pattern and Sr-Nd-Hf-Pb isotopic composition of the exposed basaltic rocks exhibit oceanic island basalt (OIB)-like characteristics, indicating an origin in the mantle (Yan et al., 2018; Zhou & Mukasa, 1997). Our tomographic result reveals two low-velocity anomalies (L1 and L2) beneath the western and southern margins of the Khorat Plateau, which coincide with the low-velocity body uncovered to the southwest of the Khorat Plateau by Li and van der Hilst (2010). The low-velocity anomalies, L1 and L2, possibly signify mantle upwelling. They may represent the source zones for the basalts observed in the southwest of the plateau, implying that the lithosphere beneath the southern and western margins of the plateau may have been modified. The presence of mantle upwelling is consistent with geodynamic simulations, which suggest that mantle convection in the South China Sea is driven by the kinematic motion of surrounding plates and mantle density-driven buoyant flows (Lin et al., 2019). Consequently, the mantle upwelling beneath the margins of the Khorat Plateau may arise from mantle convection triggered by the surrounding subduction systems of the Indo-Austrailian, Pacific, and Philippine Sea Plates (Lin et al., 2019).

Moreover, Y. Yu et al. (2017) reported a thinner mantle transition zone (MTZ) beneath the western margin of the Khorat Plateau (area B in Y. Yu et al. (2017))), which is connected with the root of the western low-velocity anomaly (L1) in our model (Figure 8b). The thinner MTZ is believed to be associated with a suggested slab window of the Indian Plate (Pesicek et al., 2008; Y. Yu et al., 2017). The detachment of the Indian subducting slab allows hot asthenospheric materials to flow up into or through the slab window, leading to mantle upwelling (Arboit et al., 2016). Thus, in addition to the mantle convection caused by subduction as discussed by Lin et al. (2019), the asthenospheric upwelling caused by the detachment of the Indian slab may also be a contributory factor to the mantle upwelling of L1. Both mechanisms are supported by the similar geochemical signatures of the basalts originating from mantle sources (Yan et al., 2018; Zhou & Mukasa, 1997).

6. Conclusions

We have developed a novel framework for teleseismic traveltime tomography based on the adjoint-state method. The tomographic inverse problem is formulated as an Eikonal equation-constrained optimization problem. The computation of ray paths is totally avoided in the forward modeling and sensitivity kernel generation, which avoids the potential failures of conventional shooting and bending methods for ray tracing and makes the computational cost nearly independent of the number of receivers. The multi-grid model parameterization and step size-controlled gradient descent method are employed to update the model parameters. The efficacy of our new method is tested using recently recorded teleseismic differential traveltime data to image the velocity structure beneath Thailand and its adjacent regions.

The tomographic result reveals a thick lithosphere beneath the Khorat Plateau and signifies mantle upwelling along its western and southern margins. The mantle upwelling is probably driven by surrounding subduction systems, with the western one possibly originating from the slab window of the Indian Plate. The presence of the mantle upwelling correlates with the source zone of erupted Cenozoic basalts, suggesting lithospheric modification beneath the southern and western margins of the plateau. Our model provides convincing evidence for the existence of mantle upwelling beneath the western and southern margins of the Khorat Plateau, offering new insights into geological dynamics in the Indochina Peninsula and validating the effectiveness of our new tomographic inversion method.

Data Availability Statement

The waveform data of the TSAR (S. Tanaka et al., 2019) can be accessed via the link: http://ohpdmc.eri.u-tokyo.ac.jp/breq-fast-tsar/index.html. The data from 11 additional permanent stations are accessible in the Incorporated Research Institutions for Seismology (IRIS) Data Management Center via the link: http://ds.iris.edu/mda/TM/PBKT/?starttime=2008-01-01&endtime=2599-12-31.

Acknowledgments
We are grateful for the editors and two anonymous reviewers for their valuable and insightful comments, which have greatly improved this paper. This work was funded by MOE AcRF Tier-2 Grant MOE-T2EP20122-0008. PT and SW were also partly supported by the National Research Foundation Singapore and the Singapore Ministry of Education under the Research Centers of Excellence Initiative (Project 04MNS001953A620). JY is supported by MOST Special Fund from the State Key Laboratory of Geological Processes and Mineral Resources, China University of Geosciences (MSFG-PMR2022-6), and the National Natural Science Foundation of China (Grant NSFC42204095).

References

Aki, K., Christoffersson, A., & Husebye, E. S. (1977). Determination of the three-dimensional seismic structure of the lithosphere. *Journal of Geophysical Research*, *82*(2), 277–296. https://doi.org/10.1029/jb082i002p00277

Arboit, F., Collins, A. S., Morley, C. K., Jourdan, F., King, R., Foden, J., & Amrouch, K. (2016). Geochronological and geochemical studies of mafic and intermediate dykes from the Khao Khwang fold–thrust belt: Implications for petrogenesis and tectonic evolution. *Gondwana Research*, *36*, 124–141. https://doi.org/10.1016/j.gr.2016.04.005

Beller, S., Monteiller, V., Operto, S., Nolet, G., Paul, A., & Zhao, L. (2018). Lithospheric architecture of the South-Western Alps revealed by multiparameter teleseismic full-waveform inversion. *Geophysical Journal International*, *212*(2), 1369–1388. https://doi.org/10.1093/gji/ggx216

Benz, H. M., Zandt, G., & Oppenheimer, D. H. (1992). Lithospheric structure of northern California from teleseismic images of the upper mantle. *Journal of Geophysical Research*, *97*(B4), 4791–4807. https://doi.org/10.1029/92jb00067

Bianchi, M., Heit, B., Jakovlev, A., Yuan, X., Kay, S. M., Sandvol, E., et al. (2013). Teleseismic tomography of the southern Puna Plateau in Argentina and adjacent regions. *Tectonophysics*, *586*, 65–83. https://doi.org/10.1016/j.tecto.2012.11.016

Chen, H., Li, Z., Luo, Z., Ojo, A. O., Xie, J., Bao, F., et al. (2021). Crust and upper mantle structure of the South China Sea and adjacent areas from the joint inversion of ambient noise and earthquake surface wave dispersions. *Geochemistry, Geophysics, Geosystems*, *22*(3), e2020GC009356. https://doi.org/10.1029/2020gc009356

Chen, J., Chen, G., Nagaso, M., & Tong, P. (2023). Adjoint-state traveltime tomography for azimuthally anisotropic media in spherical coordinates. *Geophysical Journal International*, *234*(1), 712–736. https://doi.org/10.1093/gji/ggad093

Fomel, S., Luo, S., & Zhao, H. (2009). Fast sweeping method for the factored Eikonal equation. *Journal of Computational Physics*, *228*(17), 6440–6455. https://doi.org/10.1016/j.jcp.2009.05.029

Frederiksen, A. W., Bostock, M. G., VanDecar, J. C., & Cassidy, J. F. (1998). Seismic structure of the upper mantle beneath the northern Canadian Cordillera from teleseismic travel-time inversion. *Tectonophysics*, *294*(1–2), 43–55. https://doi.org/10.1016/s0040-1951(98)00095-x

Graeber, F. M., Houseman, G. A., & Greenhalgh, S. A. (2002). Regional teleseismic tomography of the western Lachlan Orogen and the newer volcanic province, southeast Australia. *Geophysical Journal International*, *149*(2), 249–266. https://doi.org/10.1046/j.1365-246x.2002.01598.x

Hole, J. A., & Zelt, B. C. (1995). 3-D finite-difference reflection traveltimes. *Geophysical Journal International*, *121*(2), 427–434. https://doi.org/10.1111/j.1365-246x.1995.tb05723.x

Huchon, P., Pichon, X. L., & Rangin, C. (1994). Indochina peninsula and the collision of India and Eurasia. *Geology*, *22*(1), 27–30. https://doi.org/10.1130/0091-7613(1994)022<0027:ipatco>2.3.co;2

Kennett, B. L. N., & Engdahl, E. R. (1991). Traveltimes for global earthquake location and phase identification. *Geophysical Journal International*, *105*(2), 429–465. https://doi.org/10.1111/j.1365-246x.1991.tb06724.x

Kennett, B. L. N., Engdahl, E. R., & Buland, R. (1995). Constraints on seismic velocities in the Earth from traveltimes. *Geophysical Journal International*, *122*(1), 108–124. https://doi.org/10.1111/j.1365-246x.1995.tb03540.x

Laske, G., Masters, G., Ma, Z., & Pasyanos, M. (2013). Update on CRUST1.0 - A 1-degree global model of Earth's crust. In *Geophysical research abstracts* (Vol. 15, p. 2658).

Lebedev, S., & Nolet, G. (2003). Upper mantle beneath Southeast Asia from S velocity tomography. *Journal of Geophysical Research*, *108*(B1), 2048. https://doi.org/10.1029/2000jb000073

Lee, C.-T. A., Luffi, P., & Chin, E. J. (2011). Building and destroying continental mantle. *Annual Review of Earth and Planetary Sciences*, *39*(1), 59–90. https://doi.org/10.1146/annurev-earth-040610-133505

Lei, J., & Zhao, D. (2016). Teleseismic P-wave tomography and mantle dynamics beneath Eastern Tibet. *Geochemistry, Geophysics, Geosystems*, *17*(5), 1861–1884. https://doi.org/10.1002/2016gc006262

Leung, S., & Qian, J. (2006). An adjoint state method for three-dimensional transmission traveltime tomography using first-arrivals. *Communications in Mathematical Sciences*, *4*(1), 249–266. https://doi.org/10.4310/cms.2006.v4.n1.a10

Li, C., & van der Hilst, R. D. (2010). Structure of the upper mantle and transition zone beneath Southeast Asia from traveltime tomography. *Journal of Geophysical Research*, *115*(B7), B07308. https://doi.org/10.1029/2009jb006882

Li, C., van der Hilst, R. D., & Toksöz, M. N. (2006). Constraining P-wave velocity variations in the upper mantle beneath Southeast Asia. *Physics of the Earth and Planetary Interiors*, *154*(2), 180–195. https://doi.org/10.1016/j.pepi.2005.09.008

Lin, J., Xu, Y., Sun, Z., & Zhou, Z. (2019). Mantle upwelling beneath the South China Sea and links to surrounding subduction systems. *National Science Review*, *6*(5), 877–881. https://doi.org/10.1093/nsr/nwz123

Liu, S., Suardi, I., Xu, X., Yang, S., & Tong, P. (2021). The geometry of the subducted slab beneath Sumatra revealed by regional and teleseismic traveltime tomography. *Journal of Geophysical Research: Solid Earth*, *126*(1), e2020JB020169. https://doi.org/10.1029/2020jb020169

Liu, S., Suardi, I., Yang, D., Wei, S., & Tong, P. (2018). Teleseismic traveltime tomography of northern Sumatra. *Geophysical Research Letters*, *45*(24), 13–231. https://doi.org/10.1029/2018gl078610

Liu, S., Suardi, I., Zheng, M., Yang, D., Huang, X., & Tong, P. (2019). Slab morphology beneath northern Sumatra revealed by regional and teleseismic traveltime tomography. *Journal of Geophysical Research: Solid Earth*, *124*(10), 10544–10564. https://doi.org/10.1029/2019jb017625

Luo, S., & Qian, J. (2012). Fast sweeping methods for factored anisotropic Eikonal equations: Multiplicative and additive factors. *Journal of Scientific Computing*, *52*(2), 360–382. https://doi.org/10.1007/s10915-011-9550-y

Monteiller, V., Chevrot, S., Komatitsch, D., & Wang, Y. (2015). Three-dimensional full waveform inversion of short-period teleseismic wavefields based upon the SEM–DSM hybrid method. *Geophysical Journal International*, *202*(2), 811–827. https://doi.org/10.1093/gji/ggv189

Oncescu, M. C., Burlacu, V., Anghel, M., & Smalbergher, V. (1984). Three-dimensional P-wave velocity image under the Carpathian arc. *Tectonophysics*, *106*(3–4), 305–319. https://doi.org/10.1016/0040-1951(84)90182-3

Pan, Y., Liu, S., Yang, D., Wang, W., Xu, X., Shen, W., & Li, M. (2022). A review of the influencing factors on teleseismic traveltime tomography. *Earthquake Science*, *36*(3), 228–253. https://doi.org/10.1016/j.eqs.2022.12.006

Pesicek, J. D., Thurber, C. H., Widiyantoro, S., Engdahl, E. R., & DeShon, H. R. (2008). Complex slab subduction beneath northern Sumatra. *Geophysical Research Letters*, *35*(20), L20303. https://doi.org/10.1029/2008gl035262

Rawlinson, N., & Fishwick, S. (2012). Seismic structure of the southeast Australian lithosphere from surface and body wave tomography. *Tectonophysics*, *572*, 111–122. https://doi.org/10.1016/j.tecto.2011.11.016

Rawlinson, N., Hauser, J., & Sambridge, M. (2008). Seismic ray tracing and wavefront tracking in laterally heterogeneous media. *Advances in Geophysics*, *49*, 203–273.

Rawlinson, N., & Kennett, B. (2008). Teleseismic tomography of the upper mantle beneath the southern Lachlan Orogen, Australia. *Physics of the Earth and Planetary Interiors*, *167*(1–2), 84–97. https://doi.org/10.1016/j.pepi.2008.02.007

Rawlinson, N., Reading, A. M., & Kennett, B. L. (2006). Lithospheric structure of Tasmania from a novel form of teleseismic tomography. *Journal of Geophysical Research*, *111*(B2), B02301. https://doi.org/10.1029/2005jb003803

Richter, B., & Fuller, M. (1996). Palaeomagnetism of the Sibumasu and Indochina blocks: Implications for the extrusion tectonic model. *Geological Society, London, Special Publications*, *106*(1), 203–224. https://doi.org/10.1144/gsl.sp.1996.106.01.13

Saltzer, R. L., & Humphreys, E. D. (1997). Upper mantle P wave velocity structure of the eastern Snake River Plain and its relationship to geodynamic models of the region. *Journal of Geophysical Research*, *102*(B6), 11829–11841. https://doi.org/10.1029/97jb00211

Sato, K., Liu, Y., Wang, Y., Yokoyama, M., Yoshioka, S., Yang, Z., & Otofuji, Y.-I. (2007). Paleomagnetic study of Cretaceous rocks from Pu'er, western Yunnan, China: Evidence of internal deformation of the Indochina block. *Earth and Planetary Science Letters*, *258*(1–2), 1–15. https://doi.org/10.1016/j.epsl.2007.02.043

Singsoupho, S., Bhongsuwan, T., & Elming, S.-Å. (2014). Tectonic evaluation of the Indochina Block during Jurassic-Cretaceous from palaeomagnetic results of Mesozoic redbeds in central and southern Lao PDR. *Journal of Asian Earth Sciences*, *92*, 18–35. https://doi.org/10.1016/j.jseaes.2014.06.001

Steck, L. K., & Prothero, W. A., Jr. (1991). A 3-D raytracer for teleseismic body-wave arrival times. *Bulletin of the Seismological Society of America*, *81*(4), 1332–1339.

Steck, L. K., Thurber, C. H., Fehler, M. C., Lutter, W. J., Roberts, P. M., Baldridge, W. S., et al. (1998). Crust and upper mantle P wave velocity structure beneath Valles Caldera, New Mexico: Results from the Jemez teleseismic tomography experiment. *Journal of Geophysical Research*, *103*(B10), 24301–24320. https://doi.org/10.1029/98jb00750

Takemoto, K., Sato, S., Chanthavichith, K., Inthavong, T., Inokuchi, H., Fujihara, M., et al. (2009). Tectonic deformation of the Indochina Peninsula recorded in the Mesozoic palaeomagnetic results. *Geophysical Journal International*, *179*(1), 97–111. https://doi.org/10.1111/j.1365-246x.2009.04274.x

Tanaka, K., Mu, C., Sato, K., Takemoto, K., Miura, D., Liu, Y., et al. (2008). Tectonic deformation around the eastern Himalayan syntaxis: Constraints from the Cretaceous palaeomagnetic data of the Shan-Thai block. *Geophysical Journal International*, *175*(2), 713–728. https://doi.org/10.1111/j.1365-246x.2008.03885.x

Tanaka, S., Siripunvaraporn, W., Boonchaisuk, S., Noisagool, S., Kim, T., Kawai, K., et al. (2019). *Thai seismic array (TSAR) project* (Vol. 94, pp. 1–11). Bulletin of Earthquake Research Institute, University of Tokyo.

Tapponnier, P., Peltzer, G., Le Dain, A., Armijo, R., & Cobbold, P. (1982). Propagating extrusion tectonics in Asia: New insights from simple experiments with plasticine. *Geology*, *10*(12), 611–616. https://doi.org/10.1130/0091-7613(1982)10<611:petian>2.0.co;2

Tong, P. (2021a). Adjoint-state traveltime tomography: Eikonal equation-based methods and application to the Anza area in southern California. *Journal of Geophysical Research: Solid Earth*, *126*(5), e2021JB021818. https://doi.org/10.1029/2021jb021818

Tong, P. (2021b). Adjoint-state traveltime tomography for azimuthally anisotropic media and insight into the crustal structure of central California near Parkfield. *Journal of Geophysical Research: Solid Earth*, *126*(10), e2021JB022365. https://doi.org/10.1029/2021jb022365

Tong, P., Li, T., Chen, J., & Nagaso, M. (2024). Adjoint-state differential arrival time tomography. *Geophysical Journal International*, *236*(1), 139–160. https://doi.org/10.1093/gji/ggad416

Tong, P., Yang, D., & Huang, X. (2019). Multiple-grid model parametrization for seismic tomography with application to the San Jacinto fault zone. *Geophysical Journal International*, *218*(1), 200–223. https://doi.org/10.1093/gji/ggz151

Tsai, Y.-H. R., Cheng, L.-T., Osher, S., & Zhao, H.-K. (2003). Fast sweeping algorithms for a class of Hamilton–Jacobi equations. *SIAM Journal on Numerical Analysis*, *41*(2), 673–694. https://doi.org/10.1137/s0036142901396533

VanDecar, J. C., & Crosson, R. S. (1990). Determination of teleseismic relative phase arrival times using multi-channel cross-correlation and least squares. *Bulletin of the Seismological Society of America*, *80*(1), 150–169.

Vidale, J. (1988). Finite-difference calculation of travel times. *Bulletin of the Seismological Society of America*, *78*(6), 2062–2076.

Wang, K., Wang, Y., Song, X., Tong, P., Liu, Q., & Yang, Y. (2022). Full-waveform inversion of high-frequency teleseismic body waves based on multiple plane-wave incidence: Methods and practical applications. *Bulletin of the Seismological Society of America*, *112*(1), 118–132. https://doi.org/10.1785/0120210094

Weiland, C. M., Steck, L. K., Dawson, P. B., & Korneev, V. A. (1995). Nonlinear teleseismic tomography at Long Valley Caldera, using three-dimensional minimum travel time ray tracing. *Journal of Geophysical Research*, *100*(B10), 20379–20390. https://doi.org/10.1029/95jb01147

Wu, S., Yu, Y., Yang, T., Xue, M., Tilmann, F., & Chen, H. (2022). Crustal structure of the Indochina Peninsula from ambient noise tomography. *Journal of Geophysical Research: Solid Earth*, *127*(5), e2021JB023384. https://doi.org/10.1029/2021jb023384

Yan, Q., Shi, X., Metcalfe, I., Liu, S., Xu, T., Kornkanitnan, N., et al. (2018). Hainan mantle plume produced late Cenozoic basaltic rocks in Thailand, Southeast Asia. *Scientific Reports*, *8*(1), 1–14. https://doi.org/10.1038/s41598-018-20712-7

Yang, T., Liu, F., Harmon, N., Le, K. P., Gu, S., & Xue, M. (2015). Lithospheric structure beneath Indochina block from Rayleigh wave phase velocity tomography. *Geophysical Journal International*, *200*(3), 1582–1595. https://doi.org/10.1093/gji/ggu488

Yao, J., Liu, S., Wei, S., Hubbard, J., Huang, B.-S., Chen, M., & Tong, P. (2021). Slab models beneath central Myanmar revealed by a joint inversion of regional and teleseismic traveltime data. *Journal of Geophysical Research: Solid Earth*, *126*(2), e2020JB020164. https://doi.org/10.1029/2020jb020164

Yu, C., Shi, X., Yang, X., Zhao, J., Chen, M., & Tang, Q. (2017). Deep thermal structure of Southeast Asia constrained by S-velocity data. *Marine Geophysical Researches*, *38*(4), 341–355. https://doi.org/10.1007/s11001-017-9311-x

Yu, Y., Gao, S. S., Liu, K. H., Yang, T., Xue, M., & Le, K. P. (2017). Mantle transition zone discontinuities beneath the Indochina Peninsula: Implications for slab subduction and mantle upwelling. *Geophysical Research Letters*, *44*(14), 7159–7167. https://doi.org/10.1002/2017gl073528

Zhao, D., Hasegawa, A., & Kanamori, H. (1994). Deep structure of Japan subduction zone as derived from local, regional, and teleseismic events. *Journal of Geophysical Research*, *99*(B11), 22313–22329. https://doi.org/10.1029/94jb01149

Zhao, D., Yamamoto, Y., & Yanada, T. (2013). Global mantle heterogeneity and its influence on teleseismic regional tomography. *Gondwana Research*, *23*(2), 595–616. https://doi.org/10.1016/j.gr.2012.08.004

Zhao, H. (2005). A fast sweeping method for Eikonal equations. *Mathematics of Computation*, *74*(250), 603–627. https://doi.org/10.1090/s0025-5718-04-01678-3

Zhou, P., & Mukasa, S. B. (1997). Nd-Sr-Pb isotopic, and major-and trace-element geochemistry of Cenozoic lavas from the Khorat Plateau, Thailand: Sources and petrogenesis. *Chemical Geology*, *137*(3–4), 175–193. https://doi.org/10.1016/s0009-2541(96)00162-3